ACS APPLIED MATERIALS & INTERFACES

Research Article

www.acsami.org

Conductive PVDF-HFP Nanofibers with Embedded TTF-TCNQ Charge Transfer Complex

Reshef Gal-Oz,[†] Nilesh Patil,[‡] Rafail Khalfin,[§] Yachin Cohen,[§] and Eyal Zussman*[,‡]

[†]Interdepartmental Program in Polymer Engineering, [‡]Department of Mechanical Engineering, and [§]Department of Chemical Engineering, Technion—Israel Institute of Technology, Haifa 32000, Israel

ABSTRACT: Tetrathiafulvalene-tetracyanoquinodimethane charge-transfer complex (TTF-TCNQ CTC) represents a promising organic conductive system. However, application of this donor—acceptor pair is highly limited, because of its ultrafast crystallization kinetics and very low solubility. In this work, conductive organic nanofibers were generated via a coelectrospinning process of poly(vinylidene fluoride-co-hexafluoropropylene) (PVDF-HFP) with embedded TTF and TCNQ in the shell and core solutions, respectively. Upon supply of the polymer solutions, a core—shell droplet was formed at the exit of the spinneret. The electron donor TTF and the electron acceptor TCNQ migrated toward each other, within the compound droplet, to produce conductive CTC crystals. In the presence of a sufficiently strong electric field, jetting set in at the droplet tip, which yielded solidified PVDF-HFP nanofibers embedded with aligned CTC. Fiber diameters ranged between 100 and 500 nm. X-ray analysis showed strong equatorial reflections (110,200) of oriented copolymer PVDF-HFP crystals (β-phase) with copolymer chains oriented along the fiber axis, and of CTC (001), indicating that the CTC molecular planes were aligned parallel to the nanofiber axis. In addition, reflections of unreacted TCNQ (120,220) and TTF (110) crystals were observed. The electrospun nanofibers were collected to form a fiber mat, which was evaluated as a working electrode in a three-electrode cell system, exhibiting differential conductance of 5.23 μmho.

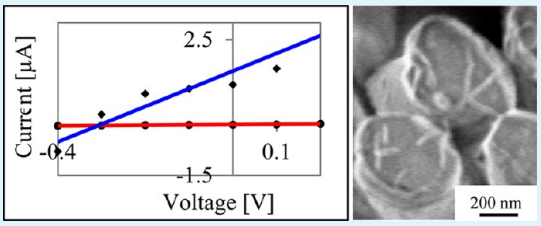

KEYWORDS: *conductivity, electrospinning, polymer, TTF-TCNQ, nanofibers, X-ray*

INTRODUCTION

The electronic conductivity of organic molecules is dictated by their ability to overcome the band gap and to transfer an electron from highest occupied molecular orbital to lowest unoccupied molecular orbital (HOMO to LUMO), and along the conductive chain. One of the most studied systems is the tetrathiafulvalene-tetracyanoquinodimethane charge-transfer complex (TTF-TCNQ CTC) (Figure 1).[1−3] The electrical conductivity of the CTC, at room-temperature, is in the range of 1×10^3 to 1×10^4 S cm^{-1}, whereas the TTF and TCNQ, as single components, are nonconductive.[4] In addition, the two components are soluble in a variety of organic solvents, whereas the CTC, which is formed rapidly at room temperature, has relatively low solubility in both polar and nonpolar solvents.[5]

The high conductivity of TTF-TCNQ CTC is attributed to a "herring bone"-type crystal structure formed by the flat TTF and TCNQ, in which orbitals on adjacent molecules overlap to form continuous one-dimensional bands. The electrical conductivity of the TTF-TCNQ couple depends on the spontaneous formation of appropriate segregated stacks of donors and acceptors, separated by less than 2 nm,[6] and on a certain degree of charge transfer between the stacks. The complex is electrically conductive over a wide range of temperatures, from 350 K down to 59 K, with a sharp metal-to-insulator transition observed at 59 K.[3]

Despite these qualities, application of TTF-TCNQ in "plastic electronics" is highly limited, because of its poor processability as a result of its ultrafast crystallization kinetics and very low solubility. Odom et al.[4] explored the formation of TTF-TCNQ CTC via mechanical rupture of microencapsulated solutions of its individual components in poly(urea formaldehyde) and found that the resulting complex has the ability to partially restore the conductivity of severed gold electrodes. Liu et al.[7] prepared TTF-TCNQ CTC nanowires and dendrites of various morphologies, using a two-phase method, in which the individual components were individually dissolved in copper and silver solutions and then recrystallized together at various temperatures. Electrical measurements of individual TTF-TCNQ nanowires indicated that the helical nanowire conducts along its *b*-axis, with a conductivity of 295 S cm^{-1}. Braun et al.[8] studied, by means of ultraviolet photoelectron spectroscopy (UPS), the organic heterojunctions in multilayered thin film stacks comprised of alternating layers of TTF and TCNQ. They showed that energy level alignment at the organic—organic interfaces in the stacks depended solely upon the relative energy structure of the donor and acceptor molecules. Recently, Mukherjee et al.[9] presented fabrication of high-performance organic thin film transistors (OTFTs) with a solution-processed TTF-TCNQ CTC film serving as bottom contact source and drain electrodes. The organic charge

Received: March 6, 2013
Accepted: June 10, 2013
Published: June 10, 2013

   dx.doi.org/10.1021/am400834b | *ACS Appl. Mater. Interfaces* 2013, 5, 6066−6072

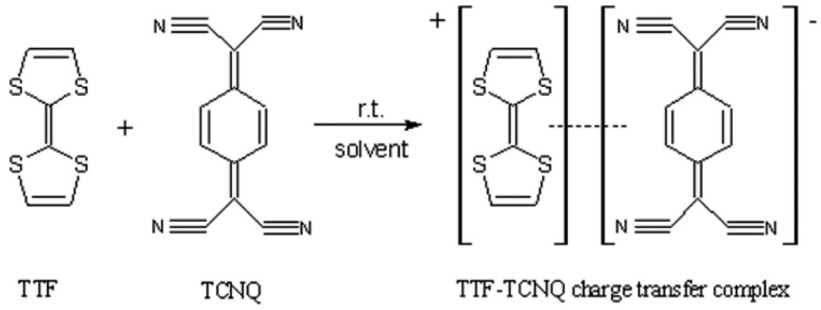

Figure 1. Formation of the TTF-TCNQ charge-transfer complex.

transfer film was deposited as contact electrodes using a capillary-based method. They found that the low work function of the TTF-TCNQ electrode and good contact of the CTC film with the organic thin film, arising from the organic–organic interface, resulted in efficient charge transfer to the semiconductor, yielding high device performance. Conductivity was not reported, however thinner films (100 μm thick) provided better electrical performance when compared to thicker films (1–5 mm thick).

Electrospinning provides an efficient means for fabrication of nanofibers with high surface area.[10,11] In this method, a charged polymer solution is drawn out into a jet and introduced into a strong electrostatic field, forcing the jet to undergo extensive stretching and thinning. As a result of an extension rate on the order of 1000 s^{-1}, alongside rapid evaporation of the solvent, ultrathin nanofibers are formed within milliseconds. The morphology of the electrospun fibers is governed by several parameters, such as the applied voltage, needle-to-collector distance, feed rate of solution, temperature, humidity, as well as the properties of the polymer solution, such as electrical conductivity, surface tension, viscosity, viscoelasticity, solvent volatility, and chemical compatibility between the polymer and the solvent. The high specific surface area of nanofibers is valuable for many applications, including particle collection, filtration, sensors, wound dressings, tissue engineering and drug delivery. High effective surface area can enhance the conductive and catalytic properties of electrodes. Electrically conductive carbon nanofiber electrodes have been prepared via electrospinning[12,13] or solution blowing[14,15] of polymer solutions, followed by carbonization at 800–1000 °C. Various metals have been loaded before and after[13] the carbonization process, to be used as catalysts for organic reactions. However, excessive fragility and inferior mechanical properties of the resulting fiber mat limit its use in solutions, rendering it highly impractical for biological and biocompatible processes. Electrospinning of intrinsically conductive polymers (ICPs) constitutes an alternative method for fabrication of conductive nanofibers. ICPs are also known as "synthetic metals", due to their π electron backbone in the form of electron resonance along the polymer chain, much like polyenes and polyaromatics.[16,17] ICP doping can increase their electrical conductivity by several folds, in acidic conditions. However, because of the rigidity of their rodlike polymer chains, electrospinning of ICP is cumbersome. On the other hand, organic conducting materials, such as the thiophene derivative 7, 9-di (thiophen-2-yl)-8H-cyclopenta[a]-acenaphthylen-8-one, which has a donor–acceptor–donor structure, have been suspended in PEO polymer solutions and electrospun.[18] The resulting electrospun fibers can function in both acidic and alkaline solutions, where in the latter, organic conductive polymers fail to electrically respond.

To overcome the low solubility of the resulting CTC, the coelectrospinning technique was selected.[19,20] In this method, two polymer solutions are simultaneously injected, forming a core–shell droplet. By applying a high electrostatic field, the droplet is drawn out into a core–shell jet, which later solidifies into a fiber (see Figure 2). Using the coelectrospinning setup,

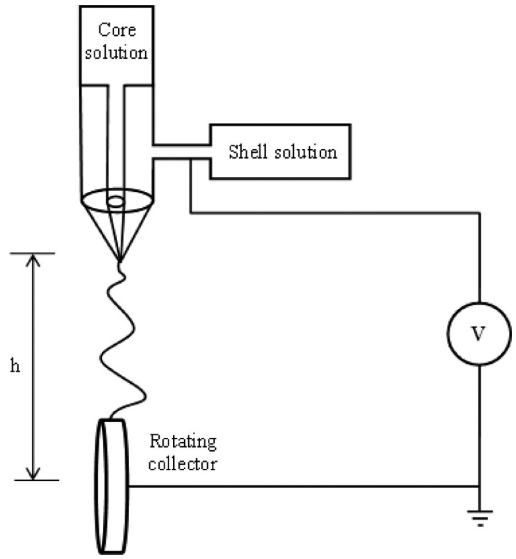

Figure 2. Schematics of the coaxial coelectrospinning process.

TTF- and TCNQ-based solutions were used to form the shell and core, respectively. TTF and TCNQ were dissolved separately in PVDF-HFP, in organic solvents (THF/DMF). The basic hypothesis was that the soluble donor (TTF) and acceptor (TCNQ) will migrate and interact during the electrospinning process, to produce the relatively insoluble CTC. Consequently, an electric conducting percolation threshold of CTC will be formed along the fibers. Critical parameters in this process which assist in controlling CTC production and its percolation threshold along the jet are: the respective flow rate of the core and shell solutions, TTF and TCNQ concentrations in the host polymer solution, the rheological properties of the host polymer solution, solvent evaporation rates, and the strength of the electrostatic field. In this work, the structure and morphology of the resulting electrospun nanofibers were studied, as well as their electrochemical activity.

EXPERIMENTAL AND PROCESS MECHANISM

Materials and Methods. All material were purchased and used as is, without further purification: PVDF-HFP (400 kDa, (Sigma

Table 1. Electrospinning Conditions of the Monolithic and Core−Shell Fibers

#system	electrospinning solution	voltage (kV)	distance h (cm)	needle o.d. (mm)	flow-rate (ml/h)
A	15 wt % PVDF-HFP in 50:50 wt % THF:DMF (stirred at RT for 1 day)	15.0	7.5	0.8	1.00
B	5 wt % TTF, 13 wt % PVDF-HFP in 50:50 wt % THF:DMF (stirred at RT for 1 day)	10.5	7.5	0.8	0.50
C	2 wt % TCNQ, 13 wt % PVDF-HFP in 50:50 wt % THF:DMF (stirred at RT for 10 days)	10.5	7.5	0.8	0.50
D1	shell solution 5 wt % TTF, 13 wt % PVDF-HFP in 50:50 wt % THF:DMF (stirred at RT for 1 day)	11.0	7.5	1.0	0.20
	core solution 2 wt % TCNQ, 13 wt % PVDF-HFP in 50:50 wt % THF:DMF (stirred at RT for 1 days)			0.8	0.20
D2	shell solution 5 wt % TTF, 13 wt % PVDF-HFP in 50:50 wt % THF:DMF (stirred at RT for 1 day)	11.0	7.5	1.0	0.20
	core solution 2 wt % TCNQ, 13 wt % PVDF-HFP in 50:50 wt % THF:DMF (stirred at RT for 10 days)			0.8	0.20

Aldrich), TTF (+99%, Acros), TCNQ (98%, S/A), tetrahydrofuran (THF) (99%, Frutarom), and dimethylformamide (DMF) (99%, Frutarom). TTF and TCNQ were coaxially electrospun in PVDF-HFP, to form TTF-TCNQ CTC-bearing nanofibers. The coaxial electrospinning setup is presented in Figure 2, where the linear speed at the edge of the disc collector was 22 m s^{-1} with an angular velocity of 1070 rpm. The coaxial electrospinning systems and process parameters are detailed in Table 1. Selection of the optimal polymer system was carried to guarantee the core−shell spinnability, while increasing the reactant (TCNQ and TTF) weight concentration.

Scanning electron microscopy (SEM) images were taken using a PHENOM SEM and Zeiss Ultra Plus HRSEM. Prior to imaging, PHENOM SEM samples were coated with a thin layer of gold. Images were taken under a vapor pressure of 0.1 mbar, using a backscatter detector, an electron acceleration voltage of 5 kV, and at a working distance of 2 mm. Zeiss Ultra Plus HRSEM images were taken without coating at an ultralow pressure of 1×10^{-7} mbar, using a secondary electron Everhart−Thornley detector, an electron acceleration voltage of 1 kV, and at a working distance of 5 mm.

Transmission electron microscope (TEM) images and an energy-dispersive X-ray (EDX) spectra were taken using an aberration-corrected monochromated FEI Titan 80−300 kV FEG S/TEM electron microscope operated at 300KeV, equipped with a Fischione HAADF-STEM detector at a high Z-contrast, and an EDX detector (Kα series EDAX AMETEK, inc.). EDX spectra were measured with a 2 nm-wide electron beam at 90°. For this purpose, fibers were collected directly on holey-carbon 300 mesh TEM copper grids.

Wide-angle X-ray scattering (WAXS) measurements of the nanofiber mats were performed using a small/wide-angle diffractometer (Molecular Metrology SAXS system with Cu Kα radiation (wavelength -0.1542 nm) from a sealed microfocus tube (MicroMax-002+S), two Göbel mirrors, and three-pinhole slits. Generator powered at 45 kV and 0.9 mA). The scattering patterns were recorded by a 15 × 15 cm two-dimensional imaging plate (BAS-IP-MS, FUJIFILM) that is positioned ~3 cm behind the sample. The scattering intensity was recorded in interval $3° < 2\theta < 68°$. Exposition time was 30 min. The sample plates under study were glued on two-dimensional holder perpendiculars to the beam, and measured under vacuum at ambient temperature. The imaging plate was scanned by Fluorescent Image Analyzing System (FLA-7000) and analyzed by FLA-7000 Image Reader software (version 10) (with 100 μm resolution).

Coaxial electrospun fiber mat ($10 \times 10 \times 1$ mm^3) performance was evaluated as a working electrode in a three-electrode cell setup (Palmsens potentiostat/galvanostat, Palm Instruments). The measurements were performed versus an Ag/AgCl reference electrode, and a platinum wire counter electrode, which were positioned 4 mm above the working electrode. Phosphate buffered saline (pH 7.4, Sigma-Aldrich) was used as an electrolyte.

Formation of Charge Transfer Complex (CTC) Embedded Nanofibers. During the coelectrospinning process, a pendant drop composed of core and shell polymer solutions is formed at the edge of the spinneret (Figure 3). A single particle residence time in the drop is defined according to drop diameter L, and the velocity $V \cong Q/L^2$;

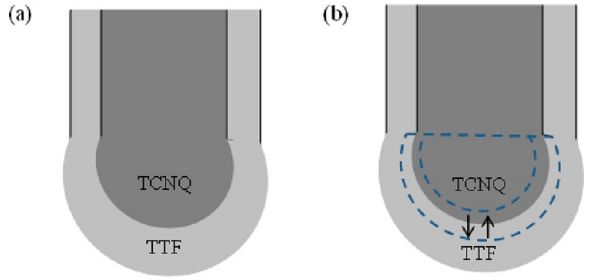

Figure 3. Scheme of the core/shell drop with the TCNQ/TTF-based solutions: (a) before initiation of an electric field, and (b) showing the respective volume components of the compound drop. The boundaries of which, noted as ΔV_{core} and ΔV_{shell}, respectively, are indicated by the dashed lines.

where Q is the solution flow rate. According to the Melcher-Taylor leaky dielectric model,[21] the diffusion time is defined by $t_d \approx L^2/D$, where D is the diffusion coefficient of the particle in medium. The diffusion time t_d is much shorter than the convection time, $t_c \approx L/V$, because $Q \ll LD$. In our case, the flow rate of both the core and shell solutions, which contain the TCNQ and the TTF, respectively is $Q = 5.56 \times 10^{-5}$ cm^3/s, and $LD \approx 2.5 \times 10^{-4}$ cm^3/s.[22] Thus, it is reasonable to assume that, the residence time, during which the TTF and TCNQ molecules exist in the compound drop, is sufficient for their meeting prior to jet formation, enabling production of CTC within the compound drop.

When applying a positive electric field, the solution's positive charge access is located at the drop-free surface, and TTF molecules (which are partially positively charged) are expected to migrate to the free surface of the drop. On a length scale of millimeter from the free surface, diffusion of both TTF and TCNQ particles is assumed to take place (Figure 3), because the intermediate region is electrically neutral (the electrical relaxation time, $t_e \approx \varepsilon/\sigma = 2.5 \times 10^{-5}$ s), and the charge transport by diffusion, electromigration, and convection are equally important.[21]

The diffusion coefficients of TCNQ and TTF molecules in the polymeric solutions are $D_{TCNQ} \approx 1 \times 10^{-5}$ cm^2/s and $D_{TTF} \approx 2 \times 10^{-5}$ cm^2/s, respectively.[22] Given the flow rate and the respective volume fraction of both solutions in the droplet, the residence time of both TTF and TCNQ is $t_c = 2.32$ s. During this time, both components concurrently diffuse across the core−shell interface, where the CTC is expected to form upon meeting, at a 100% yield. The actual quantity of the produced CTC depends on the concentration of each component in the volume fraction in the region of the core and shell drop interface. The calculated respective diffusion volumes and the final concentrations of each of the components are $\Delta V_{core} = 4.9 \times 10^{-6}$ cm^3, $\Delta V_{shell} = 6.7 \times 10^{-6}$ cm^3 and $C_{TCNQ} = 0.0979$ M, $C_{TTF} = 0.2446$ M, respectively. Thus, when calculating the diffused fraction of each of the reactants, production of 1.27×10^{-8} mol CTC in a volume fraction of approximately 8.5% from the compound drop initial volume is expected.

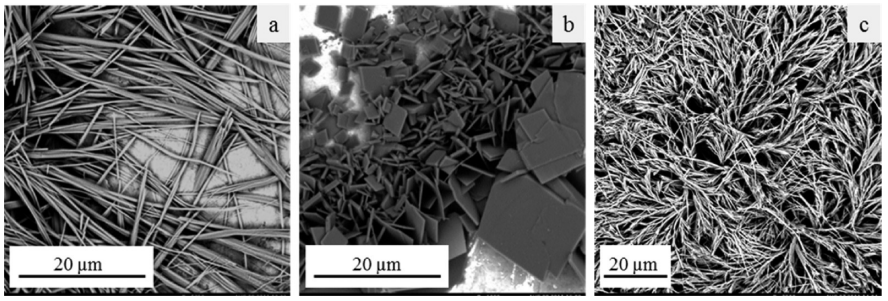

Figure 4. SEM images of recrystallization of TTF and TCNQ in organic solution (THF/DMF): (a) TTF needles, (b) TCNQ parallelograms, and (c) CTC in the form of helical dendrites.

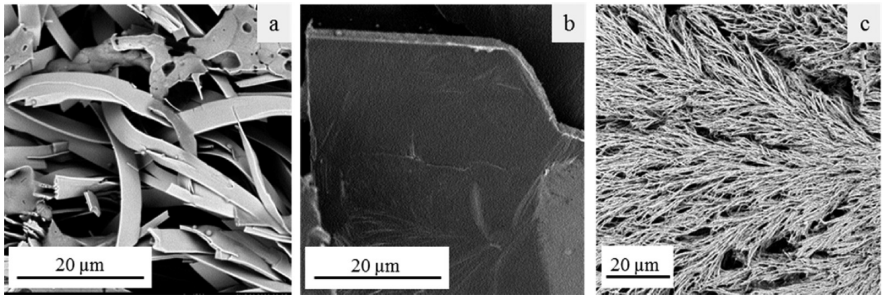

Figure 5. SEM images of recrystallization of TTF and TCNQ in a polymeric solution (PVDF-HFP in THF/DMF): (a) TTF needles, (b) TCNQ parallelograms, and (c) CTC in the form of helical dendrites.

RESULTS AND DISCUSSION

Morphology. The recrystallization of solutions of TTF, TCNQ (2 wt % TTF, and 2 wt % TCNQ in 50:50 wt % THF:DMF and 15 wt % PVDF-HFP), with and without PVDF-HFP, were studied in order to evaluate crystal morphologies in different medias. The solutions were dropped directly on a SEM aluminum stab and left to dry at room temperature. SEM images of recrystallized TTF and TCNQ solutions are presented in Figure 4, and those of recrystallized TTF and TCNQ in polymeric solution, are presented in Figure 5.

Needlelike crystals were observed when TTF recrystallized from an organic solution (Figure 4a), whereas ribbonlike crystals were obtained when recrystallized from a polymeric solution (Figure 5a). Parallelogram-like crystals were observed when TCNQ recrystallized from both organic (Figure 4b) and polymeric (Figure 5b) solutions, although an approximate 4-fold increase in area was noted when recrystallized from polymeric solution. The increase in crystal size can be attributed to the lower diffusion in the more viscous polymer solutions which affects nucleation and crystal growth. The CTC recrystallized to helical dendrites[7] from both types of solution (Figures 4c and 5c), where a more dense and thin structure was observed upon recrystallization from a polymeric solution.

Microstructure Analysis. Figure 6 shows the WAXS pattern of core/shell nanofibers formed from coelectrospun system D2 (TTF+TCNQ with PVDF-HFP). Strong equatorial reflections (110, 200) indicate the presence of oriented copolymer PVDF-HFP crystals (β-phase) with copolymer chains oriented along the fiber axis. Similar conversion of the typically occurring α-phase (antipolar phase) to the β-phase (polar phase) was previously observed in PVDF-HFP, under a high electric field and stretching.[23−25] This phase conversion occurs because of 180° rotation of antipolar alternate chains to the series of polar parallel chains. Such a transformation may have significant implications on formation of oriented

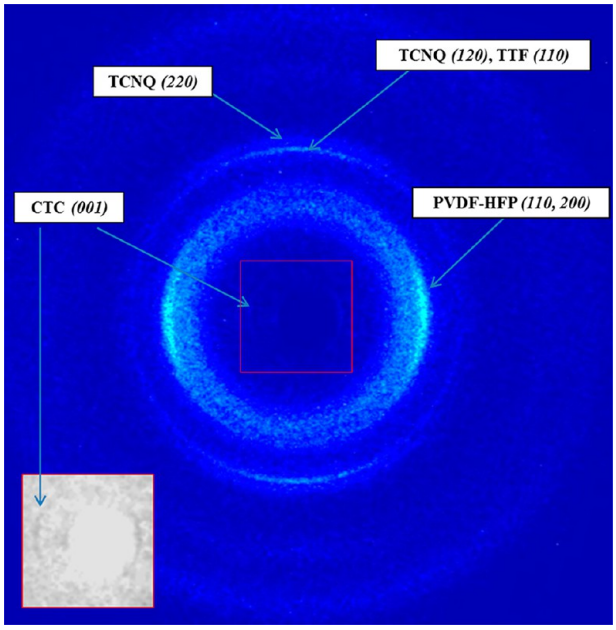

Figure 6. Wide-angle X-ray diffraction pattern of core/shell nanofiber mats prepared from system D solutions. The arrows mark off-meridional and equatorial reflections resulting from the PVDF-HFP, the CTC and the unreacted reactants TCNQ and TTF (the fiber axis is vertical).

structures with improved mechanical properties. Two strong meridional reflections illustrate the two reactants: (120, 220) planes of pure TCNQ crystals[26] and a (110) plane of TTF crystals.[27] These reflections demonstrate that the reactant crystals are oriented perpendicular to the fiber axis. The equatorial arcs of the (001) reflection of the CTC crystals suggest that they are oriented along the fiber axis.[28−30] These reflections were also observed in polymer systems B and C.

dx.doi.org/10.1021/am400834b | ACS Appl. Mater. Interfaces 2013, 5, 6066−6072

Dendrite-like typical CTC structures are expected to give a smooth ring, because of fully disoriented crystals. However, because of the low concentration of the CTC product, it is difficult to confirm whether it appears as dendrites or as single crystals.

Typical HR-SEM images of the free surface and cross-section individual fibers and fiber mat are presented in Figure 7. After

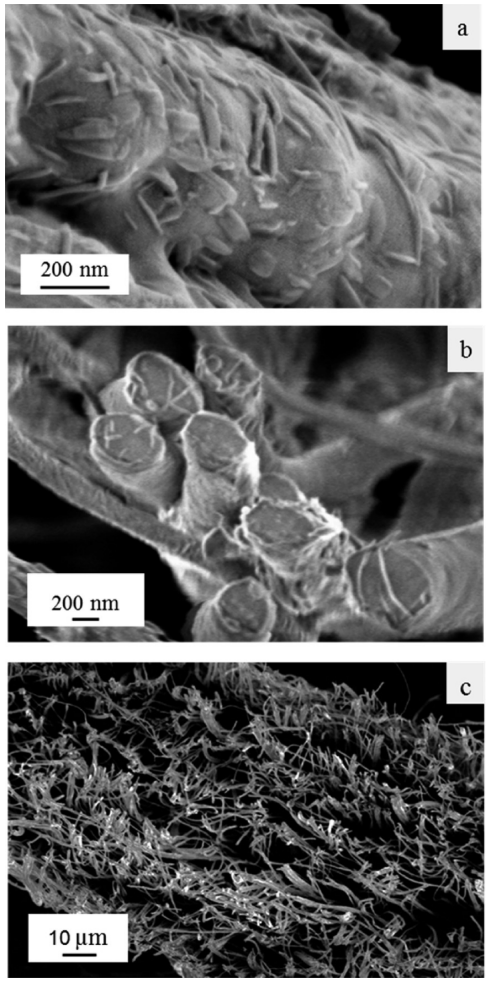

Figure 7. HR-SEM images of (a) coaxial electrospun TTF-TCNQ nanofiber free surfaces, and (b, c) cross-sections of a fiber mat.

the electrospinning process, various crystals were observed on the fiber surface and at its cross-sections. Assuming an approximate 8.5% CTC yield, obtained due to diffusion processes in the compound drop, it is expected to find three types of crystals in the electrospun fibers: crystals of the reactants (TTF and TCNQ) and of the product (CTC). TEM images and EDX spectra of these fibers shed further light on the source of these crystals; (see Figure 8a–d and Table 2).

Figure 8a–c and the recorded EDX spectra (Table 2, point #1) demonstrate the presence of a number of CTC needlelike crystals, which lay in parallel to the fiber major axis. As discussed above, CTC formation takes place in the compound drop, prior to jet formation. Once the drop elongates and a jet is formed, the jet undergoes extensive stretching and thinning, accompanied with massive evaporation of the solvent. This process leads to elongational flow,[10,20,31] which results, as expected, in ordering of the needlelike particles along with the jet axis. Figure 8d (point #3) shows that phase separation is

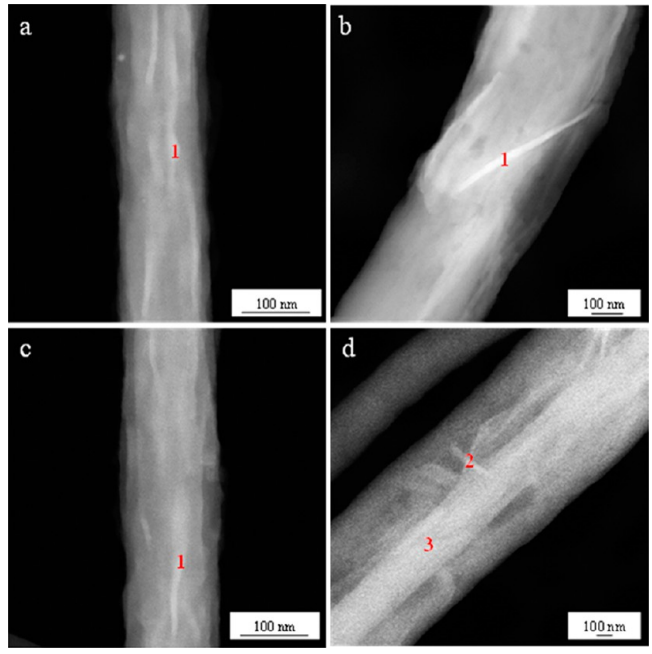

Figure 8. TEM fiber images showing the CTC needlelike crystals (a–c) arranged along the fiber's major axis, and (d) exhibiting a phase separation of core and shell. The numbers indicate positions sampled with EDX data, which determine the crystals origin (see Table 2).

Table 2. EDX Spectra: Normalized Counts (energy, eV) of the Marked Points in Figure 8

	carbon 2.8×10^2	fluoride 6.8×10^2	nitrogen 3.9×10^2	sulfur 2.3×10^2	main material[a]
point# 1 (counts)	1000	70	65	63	CTC
point# 2 (counts)	1000	106	37	371	TTF
point# 3 (counts)	1000	166	15	18	PVDF-HFP

[a]The main material values are based on the elemental analysis: most of the carbon source and the entire fluoride source are from the PVDF-HFP polymer (point# 3), whereas TTF is the only sulfur source (point# 2), TCNQ is the only nitrogen source, and the sulfur/nitrogen ratio in the CTC is 1:1 (point# 1).

formed in the fibers, with a core that is primarily composed of the PVDF-HFP polymer. Such a phase separation could be related to the radial contraction and concentration of the stretched polymer matrix,[32,33] which is typically presented as an interconnected network of subchains. The CTC and the unreacted TTF and TCNQ crystals are consequently expected to be expelled toward the fiber surface. Indeed, as shown in Figure 8d (point #2), needlelike crystals indicated as TTF crystals, were detected perpendicular to the main fiber major axis. The observed phase separation could also be generated by the induced electric field[34,35] that affects the precursor core and shell solutions in the compound droplet, just before jet formation. Because the TTF is partially positively charged and is also highly soluble, with a high diffusion coefficient,[22] it is likely to migrate to the free surface of the droplet during electrospinning. Additional observations of crystals lying on the free surface of the fibers and perpendicular to the main fiber major axis are shown in Figure 7b. Unreacted TCNQ crystals are apparently also observed in Figure 7a, situated at the free surface of the fiber. Since TCNQ has limited solubility in the

polymeric solution, it is expected to phase-separate from the polymer solution before TTF does. However, direct observations of TCNQ crystals are rather difficult, because of their sensitivity to electron radiation, leading to its degradation.[36] Comparison of the morphology of the TCNQ crystals, crystallized from the precursor solution under ambient conditions (Figure 5b), to the crystals formed during electrospinning (Figure 7b) is rather difficult because of rapid kinetic crystallization during the electrospinning of small-diameter fibers.

Electrochemistry. Electrochemical measurements were performed on coelectrospun fiber mats used as a working electrode in a three-electrode electrochemical cell. The differential conductance was calculated from the ohmic-range slope of the potential window of the multistep chrono-amperommetry curve (dI/dV), measured in buffer phosphate electrolyte, vs Ag/AgCl reference electrode and a platinum wire counter electrode. Table 3 summarizes the differential conductance in mho units of three tested working electrodes: monolithic polymer fibers (system A), TCNQ core solution that was spun before a full dissolution, after 24 h stirring (system D1), and TCNQ core solution that was spun after a full dissolution of 10 days stirring (system D2). System D1 and D2 were used for the study of TCNQ dissolution influence on the differential conductance.

Table 3. Differential Conductance of Electrospun Fiber Mats

#system	dI/dV (μmho)
A	<0.01
D1	0.09 ± 0.005
D2	5.23 ± 0.005

A typical multistep chrono-amperommetry voltammogram measurements of current as a function of time collected upon scanning the working electrodes between −1.3 V and 0.7 V, at increments of 0.1 V and time intervals of 60 to 180 s, is presented in Figure 9. The potential window of the working electrode was between −0.4 V and 0.2 V. Below −0.4 V, the electrode showed reduction behavior, and above 0.2 V, the electrode showed oxidation behavior.

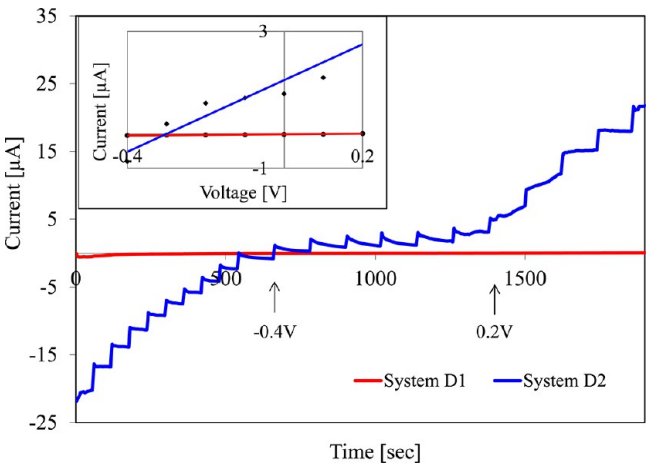

Figure 9. Multistep chrono-amperommetry voltammogram of coaxial electrospun nanofiber mats generated from systems D1 and D2. Inset: A linear fitting of the ohmic range.

The differential conductance of system D1 was found to be lower than that of system D2 by 3 orders of magnitude. As discuss above, TCNQ has limited solubility in the polymeric solution. Thus, due to the lower effective diffusion coefficient of TCNQ in solutions (compared to TTF),[22] it is assumed that its migration would determine the CTC production rate within the fiber. Therefore, the difference in the conductance can be attributed to the degree of TCNQ dissolution, where TCNQ solutions were used before a full dissolution in system D1 and after full dissolution in system D2.

The electrochemical results show that a controlled arrangement of CTC along the fibers increases the differential conductance of the electrospun fiber mat. Although at this stage the conducting mechanism is unclear, we assume that the elongational flow in the jet and finally the confinement of the CTC crystals in the electrospun fibers, affect the CTC percolation threshold. The governing factors that affect the conducting properties of aligned fiber mats are the porosity of the mats (~84%), and the average fiber diameter that determines the surface area. These parameters can be an advantage for electrochemical applications, where the liquid electrolyte can fill up the pores and support the ionic conductance between the fibers. Also, when spinning fibers from solution, local fusion may likely occur when the fibers come into contact before all solvent has evaporated from the solution. Enhanced fusion of the fibers at junctions and thus a shorter distance between these fiber-to-fiber junctions may also improve the electrical transport properties.

CONCLUSIONS

In this work, conductive organic nanofibers were fabricated in the form of core−shell nanofibers made of PVDF-HFP, with TTF and TCNQ blends in the shell and core, respectively. During the coelectrospinning process, the soluble donor (TTF) and acceptor (TCNQ) interacted in the compound droplet, forming the relatively insoluble CTC as an electric-conducting percolating network along the fibers. The content of the CTC produced within the fiber is rather low, about 1%. Analyses of the structure of the electrospun nanofibers exhibited the embedded and oriented CTC together with remains of the reactants. The differential conductance of the CTC based fiber mat was found to be 3 orders of magnitude superior to that of the neat polymer nanofiber matrix. The fiber mat can be used in various applications, for example as glucose enzymatic electrodes,[37] or as anodes in fuel cells.[13]

AUTHOR INFORMATION

Corresponding Author

*E-mail: meeyal@technion.ac.il.

Notes

The authors declare no competing financial interest.

ACKNOWLEDGMENTS

This study was partially supported by The Russel Berrie Nanotechnology Institute (RBNI). The authors would like to thank Dr. Y. Ofir for his important discussion on this manuscript, and also thank Dr. A. Arinstein for his scientific contribution.

REFERENCES

(1) Melby, L. R.; Harder, R. J.; Hertler, W. R.; Mahler, W.; Benson, R. E.; Mochel, W. E. *J. Am. Chem. Soc.* **1962**, *84*, 3374−3387.

(2) Wudl, F.; Wobschall, D.; Hufnagel, E. J. *J. Am. Chem. Soc.* **1972**, *94*, 670−672.
(3) Ferraris, J.; Cowan, D. O.; Walatka, V.; Perlstein, J. H. *J. Am. Chem. Soc.* **1973**, *95*, 948−949.
(4) Odom, S. A.; Caruso, M. M.; Finke, A. D.; Prokup, A. M.; Ritchey, J. A.; Leonard, J. H.; White, S. R.; Sottos, N. R.; Moore, J. S. *Adv. Funct. Mater.* **2010**, *20*, 1721−1727.
(5) Hiraoka, M.; Hasegawa, T.; Yamada, T.; Takahashi, Y.; Horiuchi, S.; Tokura, Y. *Adv. Mater.* **2007**, *19*, 3248−3251.
(6) Kirtley, J. R.; Mannhart, J. *Nat. Mater.* **2008**, *7*, 520−521.
(7) Liu, H. B.; Li, J. B.; Lao, C. S.; Huang, C. S.; Li, Y. L.; Wang, Z. L.; Zhu, D. B. *Nanotechnology* **2007**, *18*, 495704.
(8) Braun, S.; Liu, X.; Salaneck, W. R.; Fahlman, M. *Org. Electron.* **2010**, *11*, 212−217.
(9) Mukherjee, B.; Mukherjee, M. *Langmuir* **2011**, *27*, 11246−11250.
(10) Reneker, D. H.; Yarin, A. L.; Zussman, E.; Xu, H. *Adv. Appl. Mech.* **2007**, *41*, 43−195.
(11) Arinstein, A.; Zussman, E. *J. Polym. Sci., Part B: Polym. Phys.* **2011**, *49*, 691−707.
(12) Inagaki, M.; Yang, Y.; Kang, F. *Adv. Mater.* **2012**, *24*, 2547−2566.
(13) Prilutsky, S.; Schechner, P.; Bubis, E.; Makarov, V.; Zussman, E.; Cohen, Y. *Electrochim. Acta* **2010**, *55*, 3694−3702.
(14) Chen, S. L.; Hou, H. Q.; Harnisch, F.; Patil, S. A.; Carmona-Martinez, A. A.; Agarwal, S.; Zhang, Y. Y.; Sinha-Ray, S.; Yarin, A. L.; Greiner, A.; Schroder, U. *Energy Environ. Sci.* **2011**, *4*, 1417−1421.
(15) Dimesso, L.; Spanheimer, C.; Jaegermann, W.; Zhang, Y.; Yarin, A. L. *J. Appl. Phys.* **2012**, *111*, 064307.
(16) Lange, U.; Roznyatouskaya, N. V.; Mirsky, V. M. *Anal. Chim. Acta* **2008**, *614*, 1−26.
(17) MacDiarmid, A. G. *Rev. Mod. Phys.* **2001**, *73*, 701−712.
(18) Mishra, S. R.; Ranjith, K.; Swathi, S. K.; Ramamurthy, P. C. *Appl. Phys. Lett.* **2012**, *100*, 013302.
(19) Sun, Z. C.; Zussman, E.; Yarin, A. L.; Wendorff, J. H.; Greiner, A. *Adv. Mater. (Weinheim, Ger.)* **2003**, *15*, 1929−1936.
(20) Reznik, S. N.; Yarin, A. L.; Zussman, E.; Berkovici, L. *Phys. Fluids* **2006**, *18*, 062101.
(21) Saville, D. A. *Annu. Rev. Fluid Mech.* **1997**, *29*, 27−64.
(22) Carlsen, L.; Johansen, I.; Galster, G.; Bechgaard, K. *Ber. Bunsen-Ges. Phys. Chem. Chem. Phys.* **1980**, *84*, 458−462.
(23) Davis, G. T.; McKinney, J. E.; Broadhurst, M. G.; Roth, S. C. *J. Appl. Phys.* **1978**, *49*, 4998−5002.
(24) Newman, B. A.; Yoon, C. H.; Pae, K. D.; Scheinbeim, J. I. *J. Appl. Phys.* **1979**, *50*, 6095−6100.
(25) Dasgupta, D. K.; Doughty, K.; Brockley, R. S. *J. Phys. D: Appl. Phys.* **1980**, *13*, 2101−2114.
(26) *Powder Diffraction File Database 00-033-1889*; International Center for Diffraction Data: Newton Square, PA, 1982.
(27) Batsanov, A. S. *Acta Crystallogr., Sect. C* **2006**, *62*, O501−O504.
(28) Solovyeva, V.; Huth, M. *Synth. Met.* **2011**, *161*, 976−983.
(29) Liao, J. Y.; Ho, K. C. *Sens. Actuators, B* **2008**, *130*, 343−350.
(30) Sai, T. P.; Raychaudhuri, A. K. *Nanotechnology* **2010**, *21*, 045703.
(31) Katz, E.; Yarin, A. L.; Salalha, W.; Zussman, E. *J. Appl. Phys.* **2006**, *100*, 034313.
(32) Greenfeld, I.; Fezzaa, K.; Rafailovich, M. H.; Zussman, E. *Macromolecules* **2012**, *45*, 3616−3626.
(33) Greenfeld, I.; Arinstein, A.; Fezzaa, K.; Rafailovich, M. H.; Zussman, E. *Phys. Rev. E* **2011**, *84*, 041806.
(34) Mu, X. Y.; Liu, Y.; Fang, D. W.; Wang, Z. L.; Nie, J.; Ma, G. P. *Carbohydr. Polym.* **2012**, *90*, 1582−1586.
(35) Tsaroom, A.; Matyjaszewski, K.; Silverstein, M. S. *Polymer* **2011**, *52*, 2869−2876.
(36) Koshino, M.; Masunaga, Y. H.; Nemoto, T.; Kurata, H.; Isoda, S. *Micron* **2005**, *36*, 271−279.
(37) Gerard, M.; Chaubey, A.; Malhotra, B. D. *Biosens. Bioelectron.* **2002**, *17*, 345−359.